Journal of Superconductivity and Novel Magnetism (2021) 34:2845–2853
https://doi.org/10.1007/s10948-021-05968-x

ORIGINAL PAPER

Characterization of $CoFe_2O_4$, $NiFe_2O_4$, and $ZnFe_2O_4$ Nanoparticles Synthesized by a Proteic Sol-gel Method

M. S. Pereira[1,2] · V. M. R. Vasconcelos[2] · M. P. S. Palácio[2] · F. G. S. Oliveira[2] · L. P. M. Santos[2] · D. L. M. Vasconcelos[3] · P. T. C. Freire[3] · I. F. Vasconcelos[2]

Received: 20 May 2021 / Accepted: 12 July 2021 / Published online: 31 July 2021

Abstract
Nanoparticles of cobalt, nickel, and zinc spinel ferrites were successfully synthesized by a low-cost method named as proteic sol-gel method, and a comparative study was performed. Commercial metal nitrates and gelatin from bovine skin were used as precursors. Thermogravimetric analysis and differential scanning calorimetry were performed to investigate the thermal behavior of the precursor powders as well as to select the appropriate calcination temperature for oxide formation. Structural, morphological, optical, and magnetic properties were studied by X-ray diffraction, Mössbauer spectroscopy, transmission electron microscopy, vibrating sample magnetometry, Raman spectroscopy, and UV/VIS diffuse reflectance spectroscopy. Spherical nanoparticles with a single cubic spinel structure were obtained. The results indicate that the average particle sizes are less than 10 nm.$CoFe_2O_4$ and $NiFe_2O_4$ exhibited ferrimagnetic and superparamagnetic behavior simultaneously, whereas $ZnFe_2O_4$ was found to be paramagnetic. The optical band gaps obtained were 1.40, 1.75, and 2.12 eV for $CoFe_2O_4$, $NiFe_2O_4$, and $ZnFe_2O_4$ samples, respectively.

Keywords Spinel ferrite nanoparticles · Proteic sol-gel method · Materials caracterization · Comparative study

1 Introduction

Currently, the processing of nanomaterials that can exhibit various physicochemical properties simultaneously have attracted the interest of several research groups. Following this trend, spinel magnetic ferrite (SMF) nanoparticles (NPs) have facilitated novel advances in nanotechnology due to their remarkable properties. Technological uses of SMF-NPs included their potential applications as ferrofluids [1], in oil-spill cleanup [2, 3] and microwave devices [4, 5], as biological treatment agents [6, 7] or in photocatalysis [8], purification of wastewater [9, 10] and photovoltaics [11] applications. Among a wide range of SMF, cobalt ferrite ($CoFe_2O_4$), nickel ferrite ($NiFe_2O_4$), and zinc ferrite ($ZnFe_2O_4$) were subject to valuable investigations due to their potential applications on emerging technologies [5, 7, 11].

Spinel ferrites with chemical formula MFe_2O_4 have cubic crystal structure belonging to the $Fd\bar{3}m$ space group with 56 atoms per unit cell [12, 13]. M in the spinel structure formula unit represents a divalent metal ion like Co^{2+}, Ni^{2+}, Zn^{2+} among other. In the spinel structure, O^{2-} anions are packed into a fcc lattice with metals occupying tetrahedral and octahedral sites. There are eight tetrahedral and four octahedral sites per formula unit. In a normal spinel ferrite, M ions occupy tetrahedral sites while Fe^{3+} ions occupy octahedral sites. Inverse spinel ferrites have M cations occupying octahedral sites while Fe^{3+} ions are equally distributed among octa and tetrahedral positions. In addition, intermediate cases exist and are called mixed spinel ferrites [14].

Generally, the properties of SMF-NPs can be strongly influenced by the synthesis method [15–17]. In addition, the development of simple, cost-effective, and environment friendly methods has been required. For this purpose, several synthesis methods such as sol-gel [18–22], Pechini [23], co-precipitation [1, 24], flash [9], hydrothermal [25–27], solid-state reaction [28, 29] (among others) it was successfully used in the production of SMF-NPs.

✉ M. S. Pereira
mauriciosousa@alu.ufc.br

1 Centro de Tecnologia, Centro Universitário INTA - UNINTA, Sobral, Brazil

2 Department of Metallurgical and Materials Engineering, Universidade Federal do Ceará, Fortaleza, Brazil

3 Department of Physics, Universidade Federal do Ceará, Fortaleza, Brazil

In this research work, the authors used a low-cost method called proteic sol-gel method [30] which originates from the traditional sol-gel method. A variety of nanomaterials have been synthesized with the aid of this method [11, 31, 32]. Since the method uses low-cost materials (such as nitrates and chlorides), it has been shown to be simple, efficient, and environment friendly. $CoFe_2O_4$, $NiFe_2O_4$ and $ZnFe_2O_4$ NPs were successfully produced and a comparative study of their structural, morphological, optical, and magnetic properties was performed.

2 Experimental Procedures

$CoFe_2O_4$, $NiFe_2O_4$ and $ZnFe_2O_4$ NPs were synthesized following a experimental procedure similar to that described elsewhere [11]. Figure 1 shows a simplified illustration of the proteic sol-gel method used in the production of the ferrites.

For the production of compounds, commercial $Fe(No_3)_3 \cdot 9H_2O$ (Sigma-Aldrich, 98 %), $Co(No_3)_2 \cdot 6H_2O$ (Sigma-Aldrich, 98 %), $Ni(No_3)_2 \cdot 6H_2O$ (Sigma-Aldrich, 98 %), and $Zn(No_3)_2 \cdot 6H_2O$ (Sigma-Aldrich, 98 %) were used as

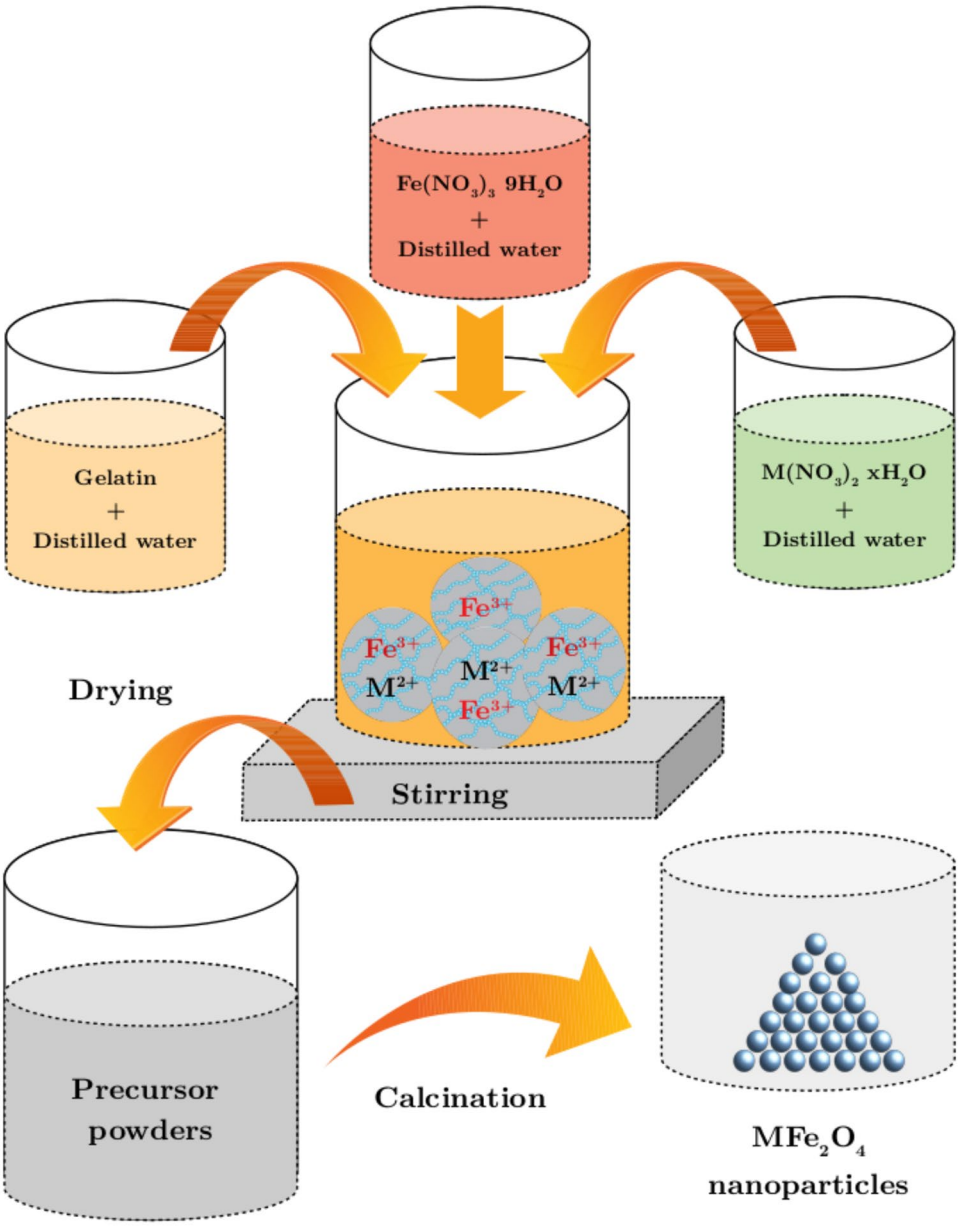

Fig. 1 Schematic representation of the proteic sol-gel method used in the production of MFe_2O_4 nanoparticles (M represents Co^{2+}, Ni^{2+} or Zn^{2+})

metal precursors (Fe^{3+}, Co^{2+}, Ni^{2+} and Zn^{2+}), whereas commercial gelatin from bovine skin (Sigma-Aldrich, Type B) as organic precursor.

The production of the ferrite NPs was performed according to the following steps: (i) the gelatin was dispersed in distilled water under continuous stirring at room temperature (RT) until a uniform gel was obtained; (ii) nitrates were dissolved in distilled water to make Co^{2+}:Fe^{3+}, Ni^{2+}:Fe^{3+}, and Zn^{2+}:Fe^{3+} solutions at a molar ratio of cobalt, nicke and zinc-to-iron of 1:2 in all cases; (iii) each metal solution was added to the gel under continuous stirring at RT for 2 h; and (iv) the resulting substances were dried at 150 °C for 6 h to remove any excess of water, resulting in a solid mass known as the precursor powder.

Prior to calcination, thermogravimetric analysis (TGA) and differential scanning calorimetry (DSC) were performed in the precursor powders in order to determine the oxide formation temperature. Based on the TGA/DSC results, the Co^{2+}:Fe^{3+}, Ni^{2+}:Fe^{3+} and Zn^{2+}:Fe^{3+} precursor powders were calcined at 400 °C for 2 h under air atmospheric conditions with a heating rate of 5 °C/min, resulting in the $CoFe_2O_4$, $NiFe_2O_4$ and $ZnFe_2O_4$ NPs.

For economy of notation, $CoFe_2O_4$, $NiFe_2O_4$ and $ZnFe_2O_4$ NPs will sometimes be referred to over this paper as CFO, NFO, and ZFO, respectively.

TGA/DSC thermal analysis were performed using a model NETZSCH STA 449F3 Jupiter equipment. The measurements were acquired under an air atmosphere applying a heating hate of 5 °C/min.

X-ray diffraction (XRD) patterns were collected using a X-Pert PRO MPD PANalytical diffractometer using a Kα-Co source ($\lambda = 1.89$ Å). The patterns were Rietveld refined [33, 34] using the GSAS software [35].

The morphology analysis of the NPs was carried out using a JEOL Jem 1011 transmission electron microscopy (TEM).

Mössbauer spectra (TMS) data were collected in standard transmission geometry at RT using a sinusoidal velocity driver with a $^{57}Co(Rh)$ radioactive source. The data were evaluated by least square fitting to series of discrete Lorentzian shaped subspectra using the software package Normos. All isomer shifts (δ) reported are relative to α-Fe.

Magnetic measurements were performed at RT using a Microsense EV9 vibrating sample magnetometer (VSM).

Raman spectroscopy were measured at RT using a HORIBA LabRam HR confocal spectrometer equipped with a N_2-cooled charge coupled device CCD detection system. A 785-nm beam of a diode laser (Coherent), with an output power of 100 mW was used as the excitation source.

Ultraviolet/visible (UV/VIS) diffuse reflectance spectroscopy was carried out on a Shimadzu UV 2600 spectrophotometer.

3 Results and Discussion

3.1 TGA/DSC Analysis

The precursor powders of the CFO, NFO, and ZFO samples were evaluated by TGA/DSC in order to determine the thermal decomposition of the compounds and to select the appropriate temperatures at which the formation of ferrites takes place. Figure 2 shows TGA/DSC curves of CFO, NFO, and ZFO obtained from the precursor powders.

From the TG analysis of the CFO precursor (see Fig. 2a), one can observe that gelatin decomposition occurs in two stages in the range between 170–310 °C resulting in a mass loss of about 50%. It also appears as two exothermic peaks at 210 and 290 °C in the DSC curve. The first stage with larger mass loss occurs in the 170–225 °C range and can be attributed to the thermal degradation of dried ferrite precursor which was initiated by oxidation/reduction reaction between nitrate and gelatin and evolution of CO_2 and NO_x gases [5, 17, 19]. This reaction is characterized by an exothermic peak at about 210 °C on the DSC scan.

The second stage is attributed to decomposition of the organic residual combustion. At this stage, formation and crystallization of corresponding metal oxides take place.

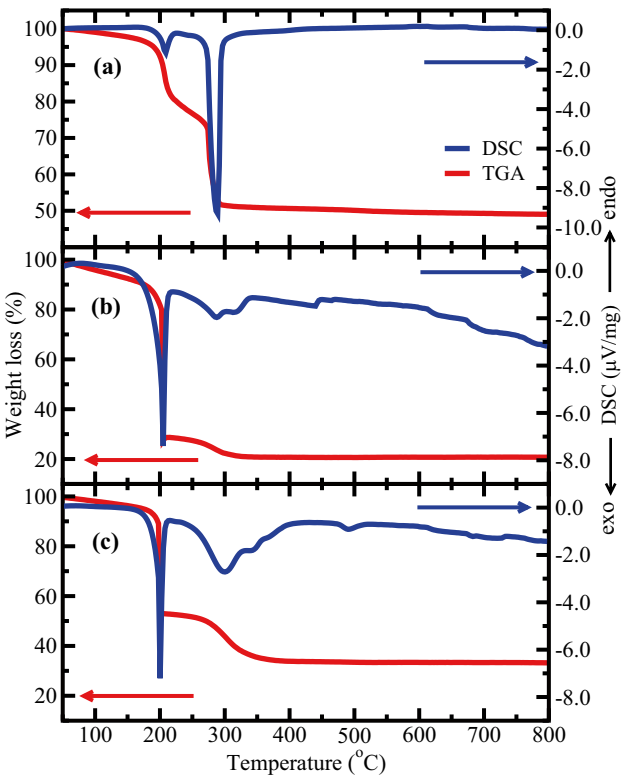

Fig. 2 TGA/DSC curves (**a**) Co^{2+}:Fe^{3+}, (**b**) Ni^{2+}:Fe^{3+} and (**c**) Zn^{2+}:Fe^{3+} precursor powders

This result is in agreement with those obtained in other works [5, 17, 19, 25]. The DSC curve does not exhibit an endothermic or exothermic processes and the TGA shows no significant mass loss above 310 °C, indicating that precursor generates a stable phase after the calcination process above this temperature.

In the case of NFO and ZFO precursor powders, similar decomposition processes are observed. Both reveal the fast decomposition (burning) of the organic part of the gelatin with mass loss about 70 and 47% for NFO and ZFO precursor powders, respectively (see Fig. 2b, c). The burning process is clearly accompanied of an exothermic effect on the DSC curve at 205 and 200 °C. The second stage occurs in the temperature range of 240–360 °C, where the burning of residual carbon takes place. Furthermore, this thermal behavior is accompanied by an exothermic effect, suggesting that the formation of NFO and ZFO oxides occur within this temperature range.

Based on these results, a calcination temperature of 400 °C was chosen for all syntheses.

3.2 X-ray Diffraction

Figure 3a shows X-ray diffraction (XRD) patterns of CFO, NFO, and ZFO samples. All diffractograms exhibit peaks that correspond to the cubic spinel structure having space group $Fd\bar{3}m$, according with the standard crystal structure 64811 (bars in Fig. 3a) obtained from Inorganic Crystal Structure Database (ICSD).

No other crystalline phase was found which attests the efficiency of the proteic sol-gel method in the yield samples that are homogeneously distributed without clustering or segregation.

XRD patterns were refined by the Rietveld method [33, 34], and the best fits are shown on the figure as solid red lines. Williamson–Hall curves [36] extracted from the data are shown on Fig. 3b. Table 1 shows structural parameters and crystallite average sizes as calculated by the Scherrer formula (D_S) and corrected by the Williamson–Hall method (D_{WH}) after compensating for residual microstrain (ϵ).

Lattice parameters (and unit cell volume) values of CFO and NFO are virtually the same while the ZFO sample exhibited slightly higher values, which is in agreement with the diffraction peak shifts toward lower 2θ values. This behavior can be explained by the difference between ionic radii of the $Co^2+ = 0.58$ Å, $Ni^2+ = 0.55$ Å and $Zn^2+ = 0.60$ ions, at octahedral or tetrahedral sites Å [37]. In general, Co^{2+} and Ni^{2+} ions tend to occupy octahedral sites while Zn^{2+} ions occupy tetrahedral sites and thus forming a inverse spinel structure. CFO, NFO, and ZFO samples showed crystallite size in the nanometer range (less than 9.0 nm) with negligible levels of microstrain.

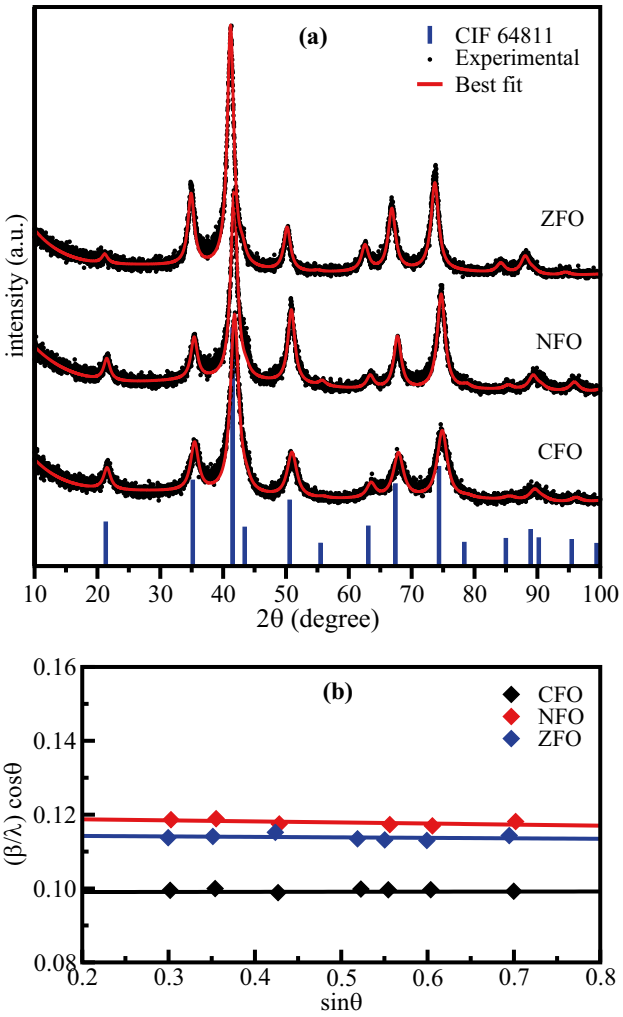

Fig. 3 (**a**) X-ray diffraction patterns of CFO, NFO, and ZFO samples. Dots and solid lines are the experimental data and best fits, respectively. Bars represent the ICSD-64811 standard pattern. (**b**) Williamson–Hall curves

3.3 Transmission Electron Microscopy

Figure 4 shows TEM images of CFO, NFO, and ZFO samples. It can be seen that CFO, NFO, and ZFO have an approximate spherical morphology with an average diameter between 5 and 11 nm, in good agreement with the sizes obtained from the XRD data.

Table 1 Lattice parameters, unit cell volume, average crystallite size, and microstrain of CFO, NFO, and ZFO samples

Sample	$a = b = c$ (Å)	Volume (Å^3)	D_S (nm)	D_{WH} (nm)	ϵ (%)
CFO	8.335	579.00	7.00	9.00	0.0090
NFO	8.345	581.89	8.50	8.40	-0.0013
ZFO	8.444	602.10	8.80	8.75	-0.0006

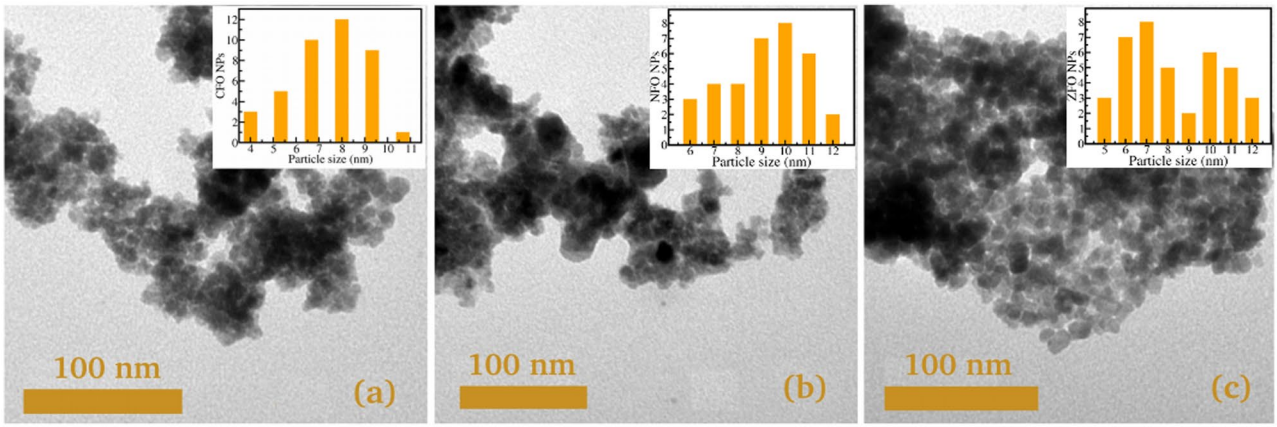

Fig. 4 TEM imagens of (**a**) CFO, (**b**) NFO, and (**c**) ZFO nanoparticles and average crystallite size distribution histograms

3.4 Mössbauer Spectroscopy

Figure 5 shows the Mössbauer spectra of the CFO, NFO, and ZTO samples taken at room temperature and the hyperfine parameters obtained from best fits for the date are summarized in Table 2.

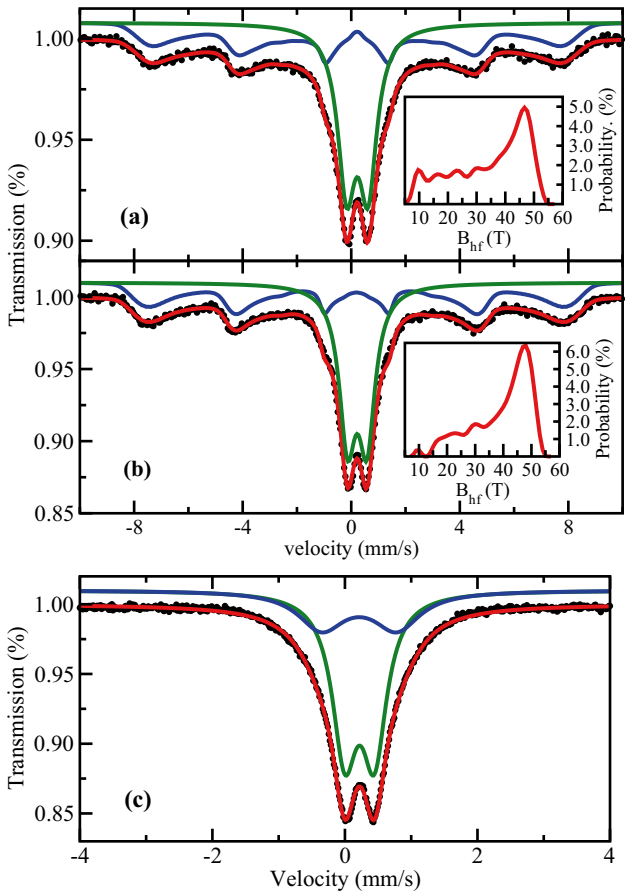

Fig. 5 Mössbauer spectra of (**a**) CFO, (**b**) NFO, and (**c**) ZFO samples with best fits to the data

Mössbauer spectroscopy is a powerful technique for assessing the of the structural and magnetic properties of a wide range of materials. Also, it may efficiently characterize the superparamagnetic behavior of nanoparticles [38]. In general, this tool enables the determination of the hyperfine interactions between nuclei and its neighboring electrons. There are three main hyperfine interactions: (i) the isomer shift (δ), which originates from the interaction between the nuclear charge and the electron density present in the nucleus, (ii) the quadrupole splitting (Δ), originating from the interaction between the quadrupole moment of the nucleus with an electric field gradient surrounding it, and (iii) the magnetic hyperfine splitting (B_{hf}), which originates from the interaction between the nuclear magnetic dipole moment with a magnetic field.

The best fits to the CFO and NFO spectra (Fig. 5a, b) were achieved using paramagnetic (doublet, green line) and ferrimagnetic (sextet, blue line). The doublet was fitted with a crystalline site while the sextet with a B_{hf} distribution. The ferrimagnetic component is a superposition of a large number of sextets showing a wide variety of environments available to the iron nuclei. The probability distributions of B_{hf} are shown in the insets. On the other hand, the ZTO spectrum was fitted using two paramagnetic doublets as seen in Fig. 5c.

In general, bulk ferrite with spinel structure exhibits ferrimagnetic properties characterized by two sextets in the Mössbauer spectrum [39, 40]. However, in nanostructured materials, the magnetic properties are more complex. In Mössbauer spectroscopy studies of magnetic nanoparticles it is known that the median blocking temperature of the ferromagnetic interactions is proportional to the particle size. The median blocking temperature of a sample is usually defined as the temperature where half of the spectral area is in the sextet and the remaining area is in the doublet [41].

Table 2 Hyperfine parameters obtained from fits for Mössbauer spectra of CFO, NFO, and ZFO samples. The hyperfine parameters are: δ – isomer shift; δ – quadrupole splitting; B_{hf} – average hyperfine magnetic field. δ and Δ in mm/s, B_{hf} in Tesla (T) and area in %. Uncentainties of δ and Δ values smaller than 0.005 mm/s, Bhf value smaller than 0.5 T and of area value smaller than 0.5 %

Sample	Sextet				Doublet		
	δ (mm/s)	Δ (mm/s)	B_{hf} (T)	Area (%)	δ (mm/s)	Δ (mm/s)	Area (%)
CFO	0.320	-0.008	46.7	52.0	0.335	0.790	48.0
NFO	0.304	-0.010	48.0	53.0	0.329	0.715	47.0
	Fe^{+3} doublet 1				Fe^{+3} doublet 2		
	δ (mm/s)	Δ (mm/s)	B_{hf} (T)	Area (%)	δ (mm/s)	Δ (mm/s)	Area (%)
ZFO	0.330	0.45	**	88.0	0.330	0.950	22.0

The central doublet present in the spectra of the CFO and NFO samples is assigned to a fraction of the compound that possesses a superparamagnetic character. Thus, the CFO and NFO samples exhibit ferrimagnetic and superparamagnetic interactions simultaneously, whereas ZFO shows only superparamagnetic behavior.

Generally, in ZFO samples the preference of Zn^{2+} ions to occupy tetrahedral sites requires all Fe^{3+} ions to occupy octahedral sites in a normal spinel structure. Thus, the Fe^{3+} ions in the octahedral sublattice is surrounded by nonmagnetic ions in the tetrahedral sublattices, resulting in a paramagnetic doublet. One of the most notable features of the Mössbauer spectra is the absence of any asymmetry that would result from the simultaneous occupation of the tetrahedral and octahedral sites by iron. Hyperfine parameters (shown in Table 2) are consistent with high spin Fe^{3+} in octahedrs of oxygen vacancies nearby.

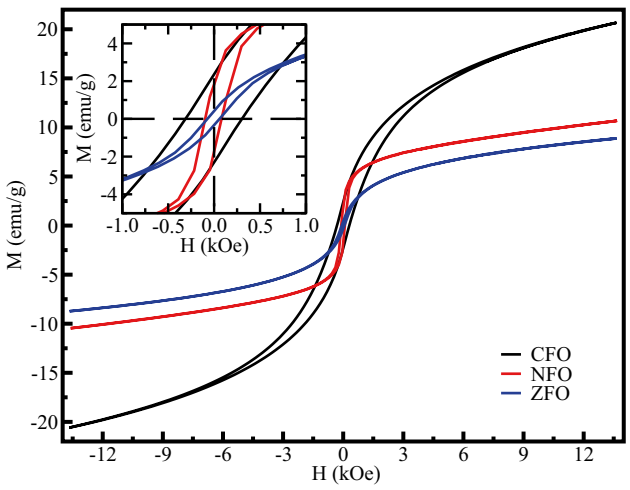

Fig. 6 Room-temperature hysteresis loops of CFO, NFO, and ZFO nanoparticles

3.5 Magnetic Properties

In general, the magnetic interactions in nanostructured magnetic materials can have a strong influence on the magnetic dynamics in samples containing ferromagnetic or ferrimagnetic nanoparticles [41]. Once the magnetic interactions in nanoparticles are unstable and disordered, the magnetic moment cannot be easily kept being consistent with the external field. Magnetic properties of magnetic nanoparticles such as remanent magnetization (M_R), maximum magnetization (M_{max}) and coercive field (H_C) are affected by cationic distribution in the sites, surface area and density. In addition, the strength of interactions between nanoparticles is very sensitive to the method of sample preparation.

Hysteresis loops taken at room temperature for CFO, NFO, and ZFO samples are shown in Fig. 6, while the corresponding magnetic parameters are reported in Table 3. It can be observed that CFO, NFO, and ZFO samples exhibited typical ferromagnetic behavior at room temperature, being more prominent in the CFO sample. However, the ZFO sample exhibit only a discrete hysteresis, indicating that this sample is predominantly paramagnetic at room temperature in agreement with the results shown by the Mössbauer spectroscopy.

Table 3 Magnetic parameter values of CFO, NFO, and ZFO samples

Sample	H_c (Oe)	M_r (emu/g)	H_{max}(emu/g)
CFO	304	2.40	18.0
NFO	90	1.80	8.50
ZFO	70	0.40	7.0

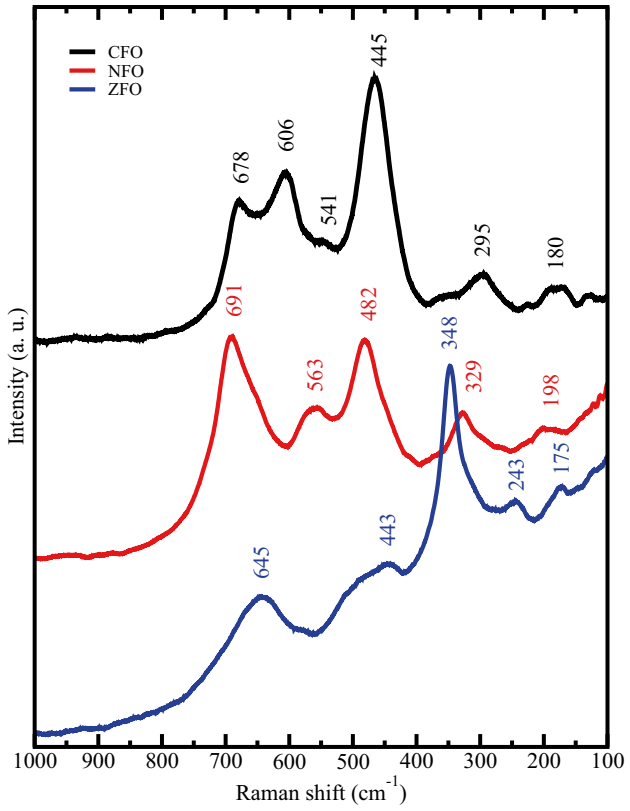

Fig. 7 Raman spectra spinel ferrite of CFO, NFO, and ZFO samples

3.6 Raman Spectroscopy

Figure 7 shows Raman spectra of CFO, NFO, and ZFO samples. Group theory analysis shows that in the center of the Brillouin Zone the 39 optical modes are distributed as $A_{1g} + E_g + T_{1g} + 3T_{2g} + 2A_{2u} + 2E_u + 4T_{1u} + 2T_{2u}$ A_{1g}, where only five of them, $A_{1g} + E_g + 3T_{2g}$, are Raman active [13].

Raman spectra of the CFO, NFO, and ZFO samples show five peaks (see Table 4) attributed to characteristic vibrational modes of the cubic spinel ferrite structure named as $A_{1g}(1)$, $T_{2g}(1)$, $T_{2g}(1)$, $E_g(2)$ and $T_{2g}(3)$. The A_{1g} mode is associated with the symmetric stretching of the oxygen anion, $T_{2g}(3)$ mode is due to the asymmetric bending of oxygen, the $T_{2g}(2)$ mode is due to asymmetric stretching of the oxygen anion with respect to the tetrahedral and octahedral cations, E_g mode is associated with symmetric bending of the oxygen anion and $T_{2g}(3)$ mode is due crystal lattice translation [12, 13].

Table 4 Raman vibrational data along with the assigned mode

Raman active mode	Observed peak (cm^{-1})			Assignment
Sample	CFO	NFO	NFO	
$T_{2g}(3)$	180	198	175	Lattice
$E_g(1)$	295	329	243	Bending
$T_{2g}(2)$	445	482	348	Bending
$T_{2g}(1)$	541	563	443	Bending
$A_{1g}(2)$	606	***	***	Stretching
$A_{1g}(1)$	678	691	645	Stretching

Regarding the CFO sample spectrum, in addition to the characteristic modes identified, a well-defined peak with a maximum around 606 cm^{-1}. This band identified as $A_{1g}(2)$ can be due to cation inversion of Co^{2+} and Fe^{3+} over the tetrahedral and octahedral sites and is consistent with recent data [8, 18, 19]. Thus, the highest frequency A_{1g} modes splits into two branches $A_{1g}(1)$ and $A_{1g}(2)$ [42, 43].

No other Raman modes which correspond to impurity phases were found, confirming the chemical quality of CFO, NFO, and ZFO compounds in agreement with the data from XRD and Mössbauer spectroscopy.

3.7 Ultraviolet/Visible Spectroscopy

Aiming to study the optical properties of the CFO, NFO, and ZFO compounds the authors used ultraviolet/visible (UV/VIS) diffuse reflectance spectroscopy. This technique allows us to evaluate relevant parameters, such as band gaps of the material, in this way, making possible a better understanding of the properties of semiconductor materials [31].

From the UV/VIS reflectance measurements can be calculated the band gap energy (E_g) of the compounds using the Kubelka–Munk (KM) method [44]:

$$F(R) = \frac{(1-R)^2}{2R}, \tag{1}$$

where R represents the reflectance and $F(R)$ the absorbance. $F(R)$ is proportional to the absorption coefficient α, given by [31]:

$$\alpha = \frac{A\,(h\nu - E_g)^n}{h\,\nu}. \tag{2}$$

wherw A is an absorption constant that depends on the material, $h\nu$ is the incident photon energy, and E_g is the optical energy band gap. The value of n fundamentally depends on the type of transition. It is equal to 1/2 for allowed direct transitions, 2 for allowed indirect transitions, 3/2 for forbidden direct transitions and 3 for forbidden indirect transitions [45]. Combining Eqs. 1 and 2, we obtain:

$$[F(R)\,h\nu]^2 \propto h\nu - E_g. \tag{3}$$

Values for E_g are obtained by extrapolating the linear part of the $[F(R)h\nu]^2 \times h\nu$ plot to the photon energy axis. This is known as the Tauc method [46].

Figure 8a shows the absorbance spectra of CFO, NFO, and ZFO samples. The CFO sample exhibits an absorption band in the infrared region while the absorption spectra of

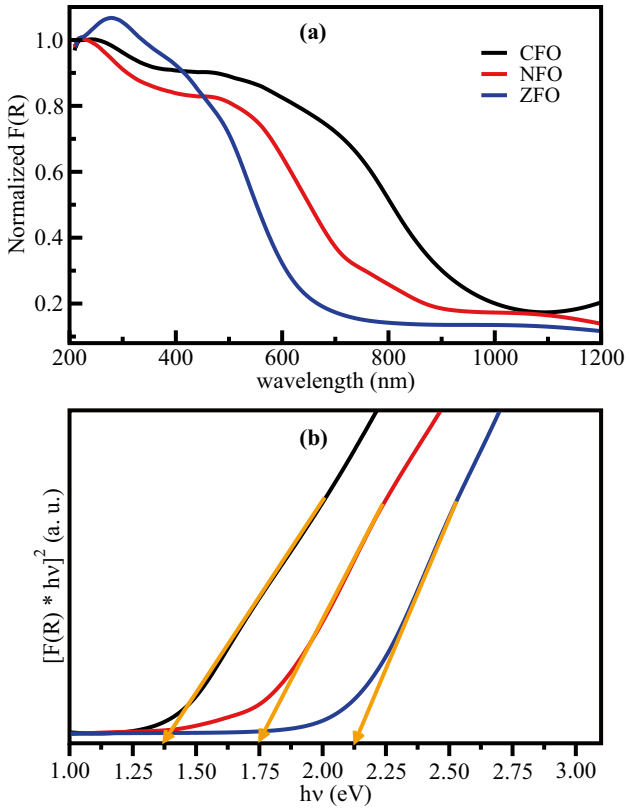

Fig. 8 (**a**) UV/VIS absorbance spectra of ZFO, NFO, and ZFO samples and (**b**) $[F(R)h\nu]^2 \times h\nu$ Tauc plots

NFO and ZFO tend to shift to lower wavelength towards the visible region.

Band gap values estimated using Tauc plots (Fig. 8b) were about 1.40, 1.75, and 2.12 eV for the CFO, NFO, and ZFO samples, respectively. These optical band gap values are in agreement with those reported by other research groups [8, 18].

4 Conclusion

The proteic sol-gel method proved to be efficient for the synthesis of $CoFe_2O_4$, $NiFe_2O_4$ and $ZnFe_2O_4$ nanoparticles. TG/DSC analysis was fundamental to estimate the temperatures formation of the ferrites.

XRD, Mössbauer, and Raman spectroscopy results for $CoFe_2O_4$, $NiFe_2O_4$ and $ZnFe_2O_4$ samples showed the presence of a single nanostructured spinel ferrite phase. Average particle sizes in the range 7.0 to 9.0 nm were estimated using XRD. TEM results showed nanoparticles with spherical shape and average diameters between 5–11 nm.

Mössbauer spectroscopy and vibrating sample magnetometry showed that $CoFe_2O_4$ and $NiFe_2O_4$ exhibit ferrimagnetic and superparamagnetic behavior simultaneously, whereas $ZnFe_2O_4$ is typically paramagnetic.

The optical band gap values estimated using UV/VIS diffuse reflectance spectroscopy were 1.40, 1.75, and 2.12 eV for the $CoFe_2O_4$, $NiFe_2O_4$ and $ZnFe_2O_4$ samples, respectively

The present work represents an evolution in the production of nanomaterials by an alternative sol-gel process and represents a promising path to applications in emerging technologies.

Funding The authors are grateful to the Brazilian research agencies Fundao Cearense de Apoio ao Desenvolvimento Cientifico Tecnologico (FUNCAP), Coordenao de Aperfeioamento de Pessoal de Nível Superior (CAPES) and Conselho Nacional de Desenvolvimento Cientifico e Tecnológico (CNPq) for financial support. The authors would also like to thank the Central Analtica-UFC/CT-INFRA/MCTI-SISNANO/Pró-Equipamentos CAPES and the X-Ray Laboratory of Federal University of Ceará for the support.

Declarations

Ethical Approval We declare that we agree with the ethical standards of the journal.

Conflict of Interest The authors declare that they have no conflict of interest.

References

1. Amirabadizadeh, A., Salighe, Z., Sarhaddi, R., Lotfollahi, Z.: Synthesis of ferrofluids based on cobalt ferrite nanoparticles: Influence of reaction time on structural, morphological and magnetic properties. J. Magn. Magn. Mater. **434**, 78–85 (2017)
2. Cardona, D.S., Debs, K.B., Lemos, S.G., Vitale, G., Nassar, N.N., Carrilho, E.N.V.M., Semensatto, D., Labuto, G.: A comparison study of cleanup techniques for oil spill treatment using magnetic nanomaterials. J. Environ. Manage. **242**, 362–371 (2019)
3. Debs, K.B., Cardona, D.S., Silva, H.D.T., Nassar, N.N., Carrilho, E.N.V.M., Haddad, P.S., Labuto, G.: Oil spill cleanup employing magnetite nanoparticles and yeast-based magnetic bionanocomposite. J. Environ. Manage. **230**, 405–412 (2019)
4. Kumar, S. J., Prameela, P., Rao, K. S., Kiran, J. N., Rao, K. H.: Structural and Magnetic Properties of Copper-Substituted Nickel–Zinc Nanoparticles Prepared by Sol-Gel Method. J. Supercond. Nov. Magn. **33**, 693–705 (2020)
5. Wang, F., Wang, X., Zhu, J., Yang, H., Kong, X., Liu, X.: Lightweight $NiFe_2O_4$ with controllable 3D network structure and enhanced microwave absorbing properties. Scientific Reports **6**, 37892 (2016)
6. Beeran, A.E., Fernandez, F.B., Nazeer, S.S., Jayasree, R.S., John, A., Anil, S., Vellappally, S., Al Kheraif, A.A., Varma, P.R.H.: Multifunctional nano manganese ferrite ferrofluid for efficient theranostic application. Colloids Surf. B: Biointerfaces **136**, 1089–1097 (2015)
7. Hoque, S.M., Hossain, M.S., Choudhury, S., Akhter, S., Hyder, F.: Synthesis and characterization of $ZnFe_2O_4$ nanoparticles and its biomedical applications. Mater. Lett. **162**, 60–63 (2016)
8. Ortiz-Quiñonez, J.L., Pal, U., Villanueva, M.S.: Structural, Magnetic, and Catalytic Evaluation of Spinel Co, Ni, and Co-Ni Ferrite Nanoparticles Fabricated by Low-Temperature Solution Combustion Process. ACS Omega **3**, 14986–15001 (2018)

9. Ramadan, R.: Physical study of cobalt ferrite and its application in purification of water. Appl. Phys. A **125**, 825 (2019)
10. Bateer, B., Tian, C., Qu, Y., Du, S., Yang, Y., Ren, Z., Pan, K., Fu, H.: Synthesis, size and magnetic properties of controllable $MnFe_2O_4$ nanoparticles with versatile surface functionalities. Dalton Trans. **43**, 9885 (2014)
11. Pereira, M. S., Lima, F. A. S., Almeida, R. Q., Martins, J. L. S., Bagnis, D., Barros, E. B., Sombra, A, S. B., Vasconcelos, I. F.: Flexible, large-area organic solar cells with improved performance through incorporation of $CoFe_2O_4$ nanoparticles in the active layer. Mater. Res. **22**, e20190417 (2019)
12. DIppolito, V., Andreozzi, G. B., Bersani, D., Lottici, P. P.: Raman fingerprint of chromate, aluminate and ferrite spinels. J. Raman Spectrosc. **46**, 1255–1264 (2015)
13. O'horo, M. P., Frisillo, A. L., White, W. B.: Lattice vibrations $MgAl_2O_4$ spinel. J. Phys. Chem. Solids **34**, 23–28 (1973)
14. Srinivas, C., Deepty, M., Kumar, E.R., Prasad, S.A.V., Tirupanyam, B.V., Meena, S.S., Prajapat, C.L., Sastry, D.L.: Rietveld refinement and FTIR spectroscopic studies of Ni^{2+} substituted Znferrite nanoparticles. Appl. Phys. A **125**, 554 (2019)
15. Rezaei, M., Mirkazemi, S.M., Alamolhoda, S.: The role of PVA surfactant on magnetic properties of $MnFe_2O_4$ nanoparticles synthesized by sol-gel hydrothermal method. J. Supercond. Nov. Magn. **34**, 1397–1408 (2021)
16. Petrova, E., Kotsikau, D., Pankov, V., Fahmi, A.: Influence of synthesis methods on structural and magnetic characteristics of Mg-Zn-ferrite nanopowders. J. Magn. Magn. Mater. **473**, 85–91 (2019)
17. Gabal, M.A., Al-Juaid, A.A., El-Rashed, S., Hussein, M.A.: Synthesis and characterization of nano-sized $CoFe_2O_4$ via facile methods: A comparative study. Mater Res Bull **89**, 68–78 (2017)
18. Yadav, R.S., Kuritka, I., Vilcakova, J., Urbánek, P., Machovsky, M., Masar, M., Holek, M.: Structural, magnetic, optical, dielectric, electrical and modulus spectroscopic characteristics of $ZnFe_2O_4$ spinel ferrite nanoparticles synthesized via honey-mediated sol-gel combustion method. J. Phys. Chem. Solids **110**, 87–99 (2017)
19. Yadav, R. S., Kuritka, I., Vilcakova, J., Havlica, J., Masilko, J., Kalina, L., Tkacz, J., Svec, J., Enev, V., Hajdúchová, M.: Impact of grain size and structural changes on magnetic, dielectric, electrical, impedance and modulus spectroscopic characteristics of $CoFe_2O_4$ nanoparticles synthesized by honey mediated sol-gel combustion method. Adv. Nat. Sci.: Nanosci. Nanotechnol. **8**, 045002 (2017)
20. Proveti, J. R. C., Porto, P. S. S., Muniz, E. P., Pereira, R. D., Araujo, D. R., Silveira, M. B.: Sol-gel proteic method using orange albedo pectin for obtaining cobalt ferrite particles. J. Sol-Gel Sci. Technol. 75, 31–37 (2015)
21. Omri, A., Dhahri, E., Costa, B.F.O., Valente, M.A.: Study of structural, morphological, Mössbauer and dielectric properties of $NiFeCoO_4$ prepared by a sol gel method. J. Sol-Gel Sci. Technol. **98**, 364–375 (2021)
22. Rekhila, G., Cherifi, K., Bessekhouad, Y., Trari, M.: Physical properties of the solid solution $NiFe_{2-x}Mn_xO_4$ prepared by sol gel. J. Sol-Gel Sci. Technol. **97**, 540–547 (2021)
23. Vlazan, P., Stoia, M.: Structural and magnetic properties of $CoFe_2O_4$ nanopowders, prepared using a modified Pechini method. Ceram. Int. **44**, 530–536 (2018)
24. Baraliya, J.D., Joshi, H.H.: Spectroscopy investigation of nanometric cobalt ferrite synthesized by different techniques. Vib. Spectrosc. **74**, 75–80 (2014)
25. Hajalilou, A., Mazlan, S.A., Abbasi, M., Lavvafi, H.: Fabrication of spherical $CoFe_2O_4$ nanoparticles via sol-gel and hydrothermal methods and investigation of their magnetorheological characteristics. RSC Adv. **6**, 89510 (2016)
26. Dhiman, M., Sharma, R., Kumar, V., Singhal, S.: Morphology controlled hydrothermal synthesis and photocatalytic properties of $ZnFe_2O_4$ nanostructures. Ceram. Int. **42**, 12594–12605 (2016)
27. Medeiros, I.A.F., Madigou, V., Lopes-Moriyama, A.L., Souza, C.P., Leroux, C.: Morphology and composition tailoring of $Co_xFe_{3-x}O_4$ nanoparticles. J. Nanopart. Res. **20**, 3 (2018)
28. Chandramohan, P., Srinivasan, M.P., Velmurugan, S., Narasimhan, S.V.: Cation distribution and particle size effect on Raman spectrum of $CoFe_2O_4$. J. Solid State Chem. **184**, 89–96 (2011)
29. El Maalam, K., Fkhar, L., Hamedoun, M., Mahmoud, A., Boschini, F., Hlil, E.K., Benyoussef, A., Mounkachi, O.: Magnetocaloric properties of zinc-nickel ferrites around room temperature. J. Supercond. Nov. Magn. **30**, 1943–1947 (2017)
30. Meneses, C.T., Flores, W.H., Garcia, F., Sasaki, J.M.: A simple route to the synthesis of high-quality NiO nanoparticles. J. Nano. Res. **9**, 501–505 (2007)
31. Pereira, M.S., Ribeiro, T.S., Lima, F.A.S., Santos, L.P.M., Silva, C.B., Freire, P.T.C., Vasconcelos, I.F.: Synthesis and properties of $Sn_{1-x}Fe_xO_2$ nanoparticles obtained by a proteic sol-gel method. J. Nano. Res. **20**, 212 (2018)
32. Pereira, M.S., Lima, F.A.S., Silva, C.B., Freire, P.T.C., Vasconcelos, I.F.: Structural, morphological and optical properties of SnO_2 nanoparticles obtained by a proteic sol-gel method and their application in dye-sensitized solar cells. J. Sol-Gel Sci. Technol. **84**, 206–213 (2017)
33. Rietveld, H.M.: Line Profiles of neutron powder-diffraction peaks for structure refinement. Acta Cryst. **22**, 151 (1967)
34. Rietveld, H.M.: A profile refinement method for nuclear and magnetic structures. J. Appl. Cryst. **2**, 65 (1969)
35. Toby, B.H.: EXPGUI, a graphical user interface for GSAS. J. Appl. Cryst. **34**, 210 (2001)
36. Williamson, G.K., Hall, W.H.: X-ray line broadening from filed aluminium and wolfram. Acta Metallurgica **1**, 22 (1953)
37. Shannon, R.D.: Revised effective ionic radii and systematic studies of interatomic distances in halides and chalcogenides. Acta Crystallogr. Sect. A **32**, 751–767 (1976)
38. El Shabrawy, S., Miglierini, M., Schaaf, P., Tzankov, D., Georgieva, M., Harizanova, R., Russel, C.: Mössbauer spectroscopy of $Zn_xMg_{1-x}Fe_2O_4$ ($0 \leq x \leq 0.74$) nanostructures crystallized from borate glasses. J. Nanopart. Res. **20**, 81 (2018)
39. Arboleda, J.D., Arnache, O., Aguirre, M.H., Ramos, R., Anadón, A., Ibarra, M.R.: Evidence of the spin Seebeck effect in Ni-Zn ferrites polycrystalline slabs. Solid State Commun. **270**, 1–7 (2018)
40. Nogueira, N.A.S., Utuni, V.H.S., Silva, Y.C., Kiyohara, P.K., Vasconcelos, I.F., Miranda, M.A.R., Sasaki, J.M.: X-ray diffraction and Mössbauer studies on superparamagnetic nickel ferrite ($NiFe_2O_4$) obtained by the proteic sol-gel method. Mater. Chem. Phys. **163**, 402–406 (2015)
41. Mørup, S., Hansen, M.F., Frandsen, C.: Magnetic interactions between nanoparticles. Beilstein J. Nanotechnol. **1**, 182–190 (2010)
42. Saccone, F.D., Ferrari, S., Errandonea, D., Grinblat, F., Bilovol, V., Agouram, S.: Cobalt ferrite nanoparticles under high pressure. J. Appl. Phys. **118**, 075903 (2015)
43. Wang, W., Ding, Z., Zhao, X., Wu, S., Li, F., Yue, M., Liu, J.P.: Microstructure and magnetic properties of MFe_2O_4 (M = Co, Ni, and Mn) ferrite nanocrystals prepared using colloid mill and hydrothermal method. J. Appl. Phys. **117**, 17A328 (2015)
44. Kubelka, P., Munk, F.: Ein beitrag zur optik der farbanstriche. Z. Tech. Phys. **12**, 593–601 (1931)
45. Davis, E. A., Mott, N. F.: Conduction in non-crystalline systems V. Conductivity and optical absorption and photoconductivity in amorphous semiconductors. Philos. Mag. A **22**, 903922 (1970)
46. Tauc, J., Grigorovici, R., Vancu, A.: Optical properties and electronic structure of amorphous germanium. Phys. Status Solidi B **15**, 627–637 (1966)